Centrifuge modeling of normal faulting and underground tunnel in sandy soil deposit

Ali Nabizadeh[1#] (ID), Alireza Seghateh Mojtahedi[2] (ID)

Article

Abstract
Earthquakes of large magnitudes cause fault ruptures propagation in soil layers and lead to interactions with subsurface and surface structures. The emergence of fault ruptures on or adjacent to the position of existing tunnels cause significant damage to the tunnels. The objective of this paper is to study the interaction of an embedded tunnel within a soil layer and the soil deformations imposed upon by normal faulting. A centrifuge modeling under 80-g acceleration was conducted to investigate the rupture propagation pattern for different relative tunnel positions. Compared with the free field condition, due to tunnel and normal fault rupture interactions, focused on soil relative density and tunnel rigidity in this research, found that they can dramatically modify the rupture path depending on the tunnel position relative to the fault tip. The tunnel diverts the rupture path to its sides. This study presents the normal fault-tunnel interaction with the tunnel axis parallel to the normal fault line, to examine the changes that take place in fault rupture plane locations, the vertical displacement of the ground surface with tunnel presence and the effect of tunnel rigidity and soil density on fault tunnel interaction.

1. Introduction

Earthquakes are potentially devastating natural events, which threaten lives, destroy properties, and disrupt life-sustaining services. The primary cause of earthquakes is the rupture of faults in the earth's crust and the associated rapid slip on these faults. In most cases, the existence of fault ruptures as well as local soil failures cause permanent ground deformations during a strong earthquake. Surface faulting is arguably the most severe seismic hazard for long lifeline facilities. For example, the fault movements of the 1999 Kocaeli and Duzce Earthquakes in Turkey were the main cause of extensive damage to the tunnel lines (Ulusay et al., 2001; Russo et al., 2002). Landslides caused by the 1930 North Izu and the 1978 Izu Oshima Island Japan earthquakes, were responsible for severe damages to the Tanna and Inatori Tunnels, respectively (Konagai et al., 2007). The 1999 Chi-Chi Earthquake in Taiwan resulted in a surface faulting of 4.0m vertical movement and severely damaged different types of tunnels (Wang et al., 2001; Konagai et al., 2007). The Wrights tunnel, a railroad tunnel crossing the San Andreas Fault, was damaged and deformed during the 1906 San Francisco earthquake (Prentice & Ponti, 1997).

The interaction of long underground structures, such as transportation tunnels, utility tunnels, oil and gas tunnels, which often cross such geological faults, with the fault rupture is still somewhat unclear for designers. Researchers found the presence of an underground structure in a soil deposit may further modify the rupture path as it propagates from the bed rock to the ground surface. Researchers have also studied on the interaction between faults and tunnels and they found that depending on the relative position of the fault tip, the tunnel longitudinal axis and the depth of the tunnel, additional axial forces and bending moments occur in the tunnel lining, which must be considered in the tunnel design (Baziar et al. 2020).

Physical modeling tests were conducted to investigate the propagation of dip-slip earthquake faults through soil layers in free field and with the presence of foundations and pipelines (e.g. Johansson & Konagai, 2004, 2006, 2007; Bransby et al., 2008a, b; Ahmed & Bransby, 2009; Loli et al., 2012; Rasouli & Fatahi, 2019; Agalianos et al. 2020; Tsatsis et al., 2019) along with numerical modeling tests (e.g. Yilmaz & Paolucci, 2007; Lin et al., 2007; Anastasopoulos et al., 2007; Loukidis et al., 2009; Baziar et al., 2012; Anastasopoulos et al., 2013; Oettle & Bray, 2013; Lee et al., 2012; Baziar et al., 2015; Tsai et al., 2015; Mortazavi Zanjani & Soroush, 2019; Thebian et al., 2018; Ghadimi Chermahini & Tahghighi, 2019). General findings include the realization that both normal and reverse fault propagations through soil is a progressive event, and

the final surface emergence of the fault rupture is dependent on soil layer depth, soil properties, dip angle and fault mode. These findings have been supported by field evidences (e.g. Kelson et al., 2004; Anastasopoulos, 2005; Bray & Kelson, 2006; Wang, 2008; Faccioli et al., 2008).

While only a few studies have reported on the interaction between tunnels and faulting events (Lin et al., 2007; Baziar et al., 2016; Naeij et al., 2019), most findings are based on field events (e.g. Wang et al., 2001 & Konagai et al., 2007). A comprehensive study of field observations from the Chi-Chi earthquake (Wang et al., 2001) showed an interaction between the faulting phenomena and tunnel. Centrifuge testing was used in other investigations to analyze the propagation of reverse faulting in single layered and multilayered soils (Tali et al., 2019), as well as the interaction of reverse faulting and tunnel lining (Baziar et al., 2014). Baziar et al. (2020) found out a shallow tunnel with less burial depth of tunnel has less internal forces than a deep tunnel due to reverse faulting displacement. Kiani et al. (2016) investigated on segmental tunnels and normal faulting by using centrifuge tests in sand layer. They found out the failure in the segmental tunnel was not sudden and tunnel lining could deviate the faulting path. Cai et al. (2019) studied on tunnel damages due to normal faulting in sand layers. They reported with the presence of a tunnel, the tunnel could act as a shielding to reduce surface settlements after normal faulting. To date, no centrifuge modeling has been conducted to investigate normal fault–tunnel interaction with the tunnel axis parallel to the normal fault line in drained sandy soil deposit.

This paper investigates tunnel performance, as embedded in soil deposit, subjected to normal dip-slip faulting using centrifuge modeling under 80-g centrifugal acceleration. The centrifuge modeling was used to allow detailed examination of the factors affecting the tunnel–fault interaction in a controlled environment and with real dimensions. The effects of burial depth, tunnel location, soil relative density and tunnel rigidity on the fault tunnel interaction have been examined within the range of tests performed in this study.

2. Experimental method

2.1 Model geometry and container

The tunnel and soil layer geometries are shown in Figure 1 schematically. A dip-slip normal fault rupture is propagated by downward displacement of the bedrock at $60°$ to the horizontal axis (α). The tunnel with the diameter of D and thickness of t, embedded in the soil layer, had a distance of (X, Y) from the fault tip, such that the tunnel was in the faulting zone obtained from the free field tests. A 60° fault dip angle was selected based on the common reported field conditions (Kelson et al., 2004; Anastasopoulos & Gazetas, 2007a, b; Faccioli et al., 2008).

2.2 Model preparation and material type

Special traveling pluviation apparatus was constructed to prepare a uniform relative density of the tested soil in the soil sample box. The sand was pluviated from specific heights, aiming to give uniform relative densities of 50-70% and soil unit weights of 15-16 kN/m³. The obtained soil is classified as poorly graded sand (SP) according to the Unified Soil Classification System. A series of direct-shear tests were conducted to investigate the soil frictional angle and cohesion, and the results of the peak frictional angles were $\varnothing = 38°$ for $D_r = 70\%$, $\varnothing = 36°$ for $D_r = 50\%$ and a secant shear modulus G of 0.5 MPa for a relative density of 55% (Lin et al., 2007; Baziar et al., 2014). The selected tested quartz sand had a specific gravity (G_s) of 2.65, maximum and minimum dry unit weights of 16.6 kN/m³ and 13.8 kN/m³, respectively, and an almost linear failure envelope and cohesion of near zero for the tested stress levels. The dilation angle of sand was $\psi = 10°$-11°. Table 1 reports the physical properties of
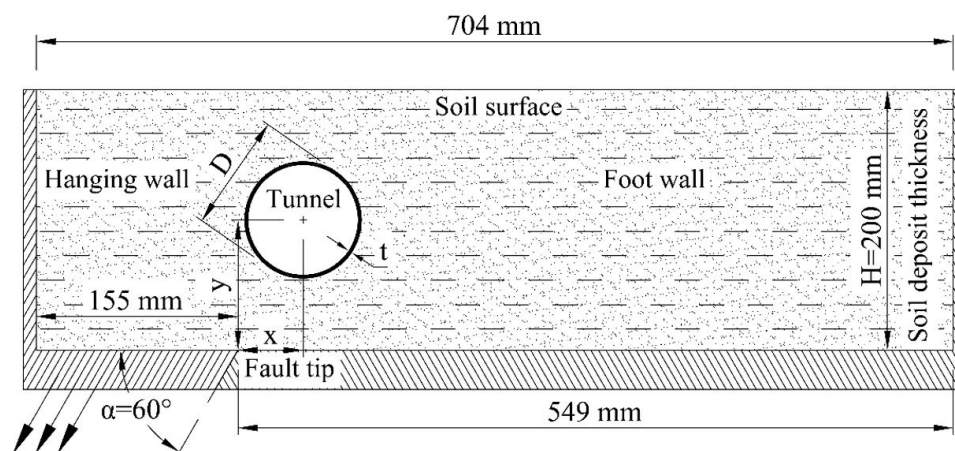
Figure 1. Schematic sketch of studied problem, indicating dimension at the model scale, interaction of normal fault rupture and tunnel.

quartz sand used in the presented study. Lee et al. (2012) reported all properties of the tested crushed quartz sand.

The tunnels were constructed from aluminum alloy (6061-T6) tubes. The external diameters of the tunnels were $D = 49.4$ and 49.8 mm and had thicknesses of $t = 1.2$ and 1.4 mm, respectively. Table 2 reports the mechanical properties of the aluminum alloy (6061-T6) used in the current tests. The external part of the aluminum tube was coated with a 0.5 mm thick LOCTITE Hysol Product epoxy to simulate the friction between the soil and tunnel. The friction between the soil and the epoxy coating, as measured from the direct shear test for the specimen with half epoxy and half sand, was about 22°. Since the resistance of the epoxy coating was very small, it did not affect the rigidity of the aluminum tube.

The well-known basic scaling law for centrifuge modeling derives from the need to ensure the similarity between the tested model and the prototype with following relationship: $(EI)_{model} * N^4 = (EI)_{prototype}$. Where N is the gravity level in the centrifuge test (in this study N = 80).

In these experiments, layers of 15 mm thick sand were initially poured and followed by 5 mm thick sand dyed with blue ink to highlight the rupture path and shear localization, observed from the front face of the soil container. Once the desired soil thickness was achieved, the aluminum tube was embedded parallel to the fault tip in the soil layer. Sand shedding was continued in the same manner until the soil deposit reached to the thickness of 200 mm.

2.3 Model instrumentation

Measurement of the surface displacement was achieved using a surface profile scanner integrated with two laser displacement transducers (LDT) and positioned on the center line of the tested sand bed during the normal faulting tests, see Figure 2b. Driving the scanner on the centerline of the fault box enables it to scan continuously the soil surface elevation. A CCD camera was installed at the front face of the acrylic plate window of the strong-box to record the soil deformation, faulting outcrop and its deviation after finishing each test. Besides, at the end of each test, soil layers were removed carefully and the tunnel movement was measured by instrumentation.

2.4 Centrifuge modeling and testing program

Figure 2b illustrates the key sketch for observing the surface rupture and distorted surface. In this figure, W indicates the distance from the bedrock fault to the location of the right side surface outcropping, α is the dip angle of the fault plane, H is the thickness of the soil deposit and h indicates the vertical offset of the fault. According to Figure 2b for studying the critical conditions, the tunnel
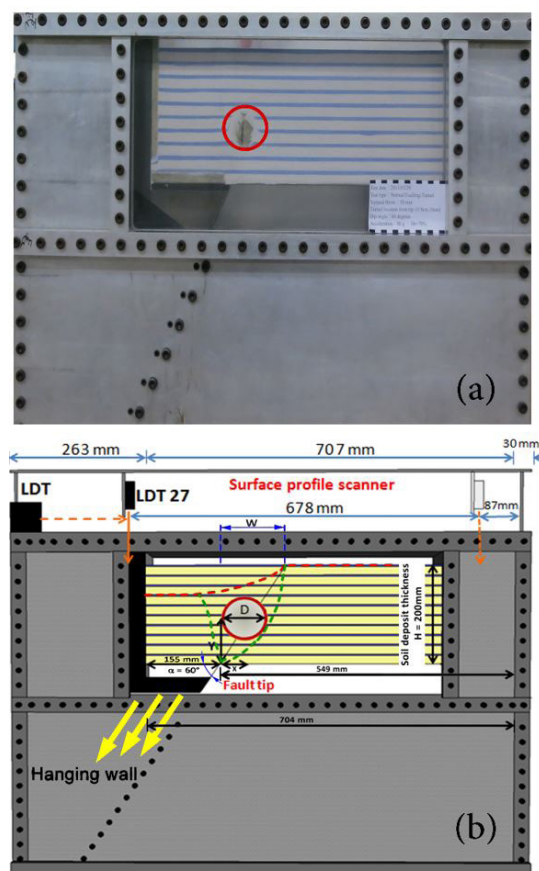
Figure 2. The centrifuge apparatus: (a) Cross section of the experimental apparatus installed in the plane strain container; (b) photograph of the apparatus and schematic diagram of the studied problem (normal fault rupture).

Table 1. Physical properties of quartz sand.

Soil Type	G_s	$\rho_{max}\left(kN/m^3\right)$	$\rho_{min}\left(kN/m^3\right)$	$d_{50}\,(mm)$	$d_{10}\,(mm)$	$\phi\;(D_r = 70\%)$
SP	2.65	16.6	13.8	0.193	0.147	38°

Table 2. Mechanical properties of the aluminum alloy used in this study (6061-T6).

Unit weight	Young's modulus	Poisson's ratio	Tensile yield stress	Tensile strength
(kN/m^3)	$E\,(GPa)$	v	$f_{yk}\,(MPa)$	$f_{bk}\,(MPa)$
27	70	0.33	500	600

was embedded part in, part outside of the fault zone in the free field test. In all tests the height of soil deposit (H) was 200 mm. In order to observe the shear zone of faulting and the tested models, an acrylic plate window was installed on the front face of the fault box. A translating base and a wall on the left side of the container simulated the normal fault with downward movement of the base and were supported by a jack serving as an actuator. The maximum stroke height using this apparatus in the normal faulting mode was 50 mm, representing a 4 m fault-displacement at the prototype scale. The downward movement (h) was increased and the vertical displacement of the surface was recorded at each increment of 2.5 mm of fault throw (equivalent of 0.2 m at the prototype scale).

The centrifuge tests were conducted at the National Central University of Taiwan. The equivalent prototype dimensions were 80 times greater than the tested model. The dimensions of the centrifuge platform were 1000 mm × 550 mm × 720 mm (length × width ×height), and the maximum payload of the platform was 400 kg at an acceleration of 100g. Lee et al. (2006, 2012) previously reported the equipment details and NCU centrifuge specifications.

A list of the tested models is shown in Table 3. Following the two free-field tests, four further tunnel tests were conducted to investigate the effects of tunnel position, tunnel depth (with dimensionless ratio of H_c/D, which H_c is the burial depth of the tunnel (Overburden pressure) and D is the diameter of the tunnel), tunnel rigidity and soil relative density.

3. Results of the centrifuge tests

3.1 Free field test with D_r =50%

Before studying the fault–tunnel interaction, it was important to investigate the behavior of normal fault propagation in dry sandy soil layer without an underground tunnel. Consequently, test 1 was conducted as a free field test for a dry sand layer of 200 mm (16 m at equivalent prototype scale) in depth and 50% in relative density.

A selection of the digital images captured after test 1 is shown in Figure 3. Figure 3a shows the image of the final fault throw at h = 50 mm (h/H = 0.25, h = 4 m at equivalent prototype scale). Figure 3b shows the digitization on the

image of the subsurface deformation profile at h = 50 mm. As seen in Figure 3b the maximum width between two fault rupture planes, visible on the soil surface, was 100 mm at the end of the test, and the final failure mechanism (right side rupture) has a displacement discontinuity with a dip angle (70◦), slightly steeper than what was applied at the base of the soil layer.

Figure 4 shows the surface deformation according to different fault throws. The fault outcropping position on the soil surface, at the end of the test (h/H = 0.25), is at X = 150 mm from fault tip shown as W parameter in the figure (W/H = 0.75). As seen in Figure 4, the surface fault outcropping starts to appear at X = 125 mm (at h/H = 0.05, or
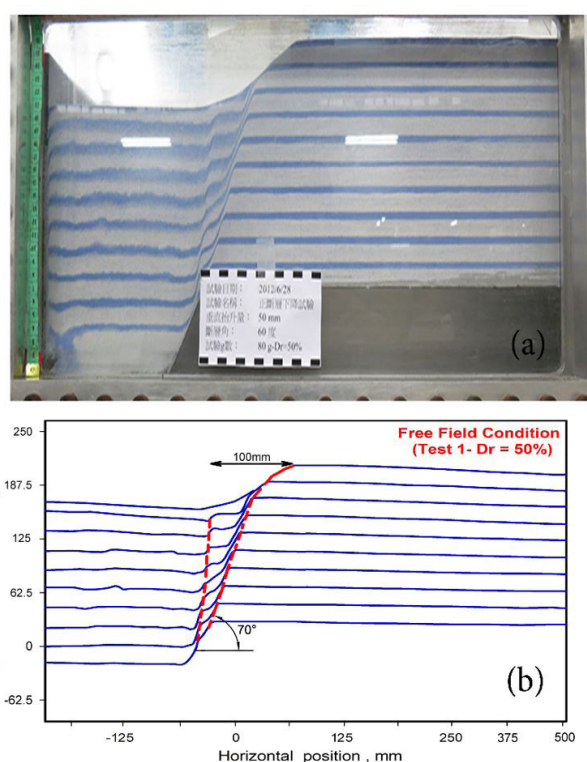
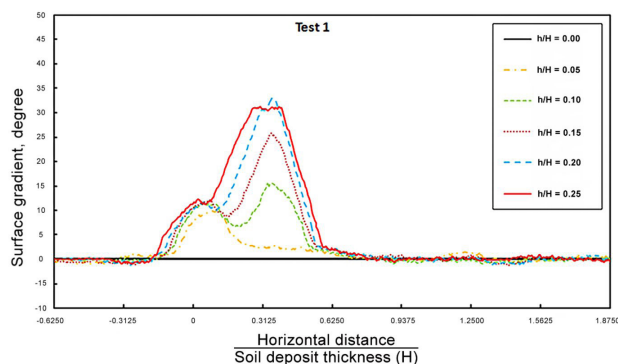**Figure 3.** Free-field normal fault rupture (test 1- $D_r = 50\%$): (a) Images of deformed soil specimen for the final fault throw; h/H = 0.25 (b) Digitization on image of subsurface deformation profile at h/H = 0.25.

Table 3. Specifications of the performed centrifuge tests for normal fault rupture.

Normal Fault rupture						
Test Number	X (mm)	Y (mm)	H_c/D	D_r (%)	Tunnel Thickness (mm)	Tunnel Diameter (mm)
1	-	-	-	50	-	-
2	-	-	-	70	-	-
3	55	130	0.92	70	1.2	49.4
4	40	100	1.52	50	1.2	49.4
5	25	75	2.03	70	1.2	49.4
6	25	75	2.01	70	1.4	49.8
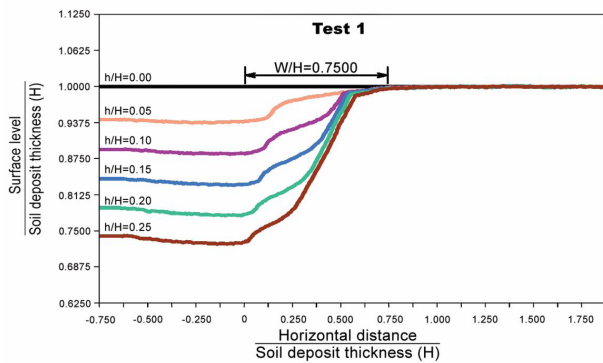
Figure 4. The ground surface level for the free-field condition for different fault throws (test 1- $D_r = 50\%$).

Figure 5. Surface gradient (ground surface inclination) against position for different fault throws (test 1).
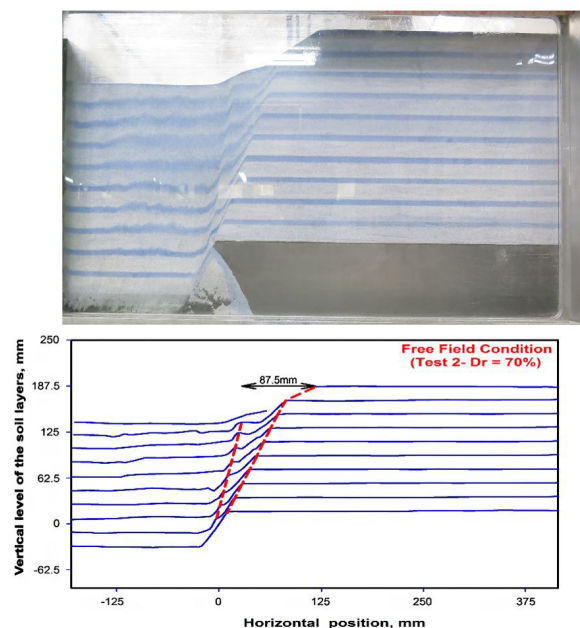
Figure 6. Free-field normal fault rupture (test 2- $D_r = 70\%$): Image of deformed soil specimen for the final fault throw; $h/H = 0.25$.

$h = 10$ mm at the model scale). A short vertical localization on the left side of the hanging wall and a longer localization (not very steep) on the right side of the soil surface observed. The same trend is observed with increasing the fault throw.

At the final vertical level of $h/H = 0.25$ (Figure 3), two rupture planes propagated in the soil layer. Figure 4 shows that propagating the fault to the ground surface at $h/H \approx 0.05$ deforms the soil surface. Finally, a fault outcropping h/H of larger than 0.10 strongly prevents further surface settlement and soil deformation, as the right and left side rupture planes are propagated up to the soil surface.

The results demonstrate that the fault propagation is a progressive phenomenon due to the ductility of the soil, as pointed out by prior researchers (e.g. Bransby et al., 2008a; Baziar et al., 2014, 2016, 2020). The initial localizations are likely to be due to high dilation behavior at small shear strains on the initial deformation of the soil layer.

Figure 5 shows that the surface gradient (ground surface inclination) width changes -75 mm $<x<$ 156 mm as the fault displacement increases. In addition, the position of the maximum surface gradient is almost constant from the base discontinuity as the fault throw increases.

## 3.2 Free field test with $D_r = 70\%$

The typical pattern of the fault rupture propagation through a dry sandy soil deposit with $D_r = 70\%$ is illustrated in Figure 6. Compared with test 1, the left rupture in test 2 is observed to be closer to the right rupture when reaching to the ground surface. A low relative density soil enables the fault movement to spread out over a wider zone than a high relative density soil similar to the reverse fault tests conducted by Baziar et al. (2014, 2016).

On the other hand, a normal fault produced rupture planes within the model ground and was propagated up to the ground surface for both tests 1 and 2. As the relative density of ground model became greater, due to the reduction of void ratio and increasing of soil mass strength, the rupture planes appeared to be closer to each other.

The vertical components of the surface displacements, as observed by analyzing the LDT results, were shown in Figure 7. As seen in Figure 7, the surface displacement discontinuity is positioned at $W/H = 0.687$, giving an angle of 40° on the soil surface.

3.3 Interaction of the normal fault rupture with tunnel

In order to examine the interaction of the tunnel and normal fault rupture, four factors were considered including the possible tunnel presence, tunnel depth, soil relative density and tunnel rigidity. The results from the four tests are presented and discussed in the following sections.
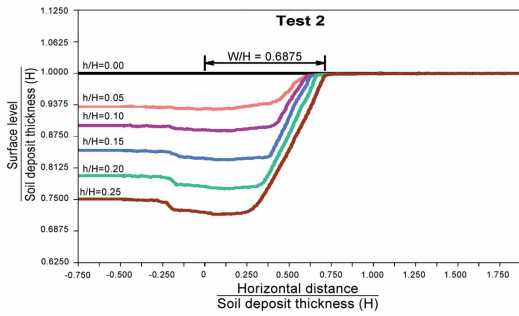
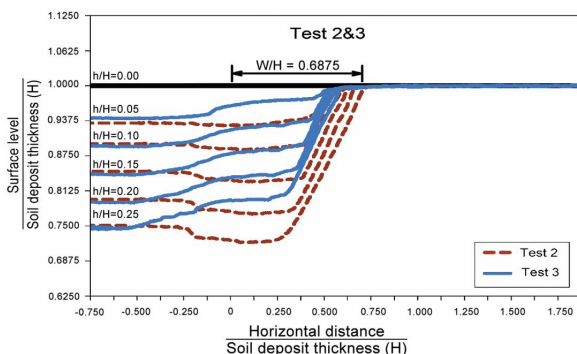**Figure 7.** The ground surface level for the free-field condition for different fault throws (test 2- $D_r = 70\%$).
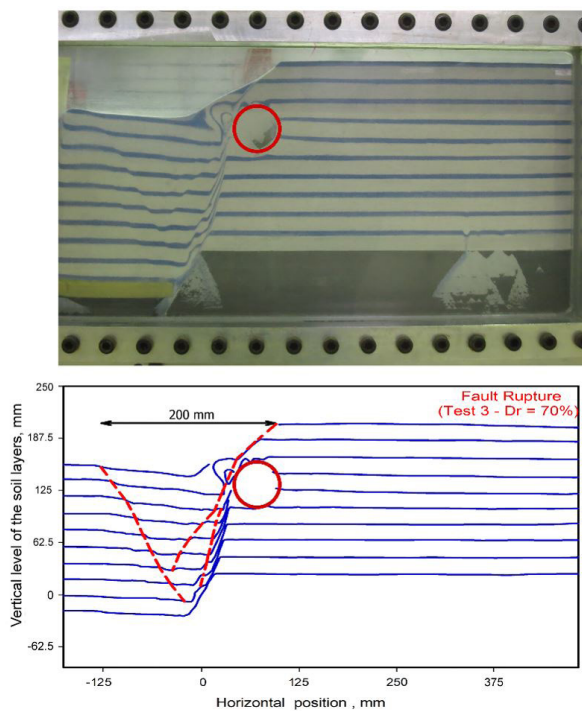
Figure 8. Tunnel test (test 3; $H_c/D = 0.92$; $X = 55$ mm; $Y = 130$ mm; $t = 1.2$ mm; $D = 49.4$ mm): Image of the deformed soil specimen for the final fault throw; $h/H = 0.25$ ($D_r = 70\%$).

Figure 9. The ground surface level with the presence of tunnel for different fault throws (test 3- $D_r = 70\%$).

3.3.1 Effect of tunnel on fault rupture path and surface displacement: base case X=55 mm, Y=130 mm

A tunnel measuring $D = 49.4$ mm in diameter and $t = 1.2$ mm in thickness ($D = 4.24$ m in diameter and $t = 0.24$ m in thickness at equivalent prototype scale) was selected as the base condition (test 3 of Table 3). These parameters were selected as typical of those expected for a medium flexible tunnel considering centrifuge scaling law. The digital image, captured at the final stage of this test ($h/H = 0.25$), is shown in Figure 8. As seen in the figure, the tunnel was embedded near the soil surface. Figure 9 shows that there are two specified localizations for small fault displacements $h/H = 0.05$. The localization for larger fault displacements ($h/H = 0.25$) was found to be very steep, similar to that observed in the free-field test. However, an observable slip plane was formed far away from the footwall side. Due to the $h/H = 0.25$ fault displacement, the right side shear plane in Figure 8 did not reach to the soil surface, and the left side shear plane propagated from the left hand edge of the tunnel before reaching the soil surface. Contrary to the free field test, the main rupture at this fault displacement does not emerge at the ground surface. A third localization for the final fault throw of $h/H \approx 0.25$ appears to propagate upwards from the displacement singularity of the tunnel's left hand edge and reaches to the surface. As seen in Figure 8, the final fault rupture emerged from the left side of the tunnel, deviating the fault rupture from the free-field case. Due to the $h/H = 0.25$ fault movement in this test, the tunnel experienced significant rotation ($\Delta\theta = 26°$) and horizontal $\Delta X = 3.8$ mm ($\Delta X = 0.3$ m at equivalent prototype scale) and vertical $\Delta Y = 6.2$ mm ($\Delta Y = 0.5$ m at equivalent prototype scale) movements. The final rotation and the final tunnel dimensions of X, Y have been measured by instrumentation after removing the sand layers very carefully at the end of each test for the final fault throw of 50 mm. The final tunnel movements also verified with the digital image analysis in the centrifuge laboratory.

Figure 8 also shows that the tunnel presence increased the distance between the shear planes to about 200 mm towards the hanging wall.

It can be observed from the Figure 9 that the position of the large deformation is very different from the deformations in the free field test. However, no further upward localization is observed on the hanging wall at $h/H > 0.05$, which is consistent with the mechanism shown in Figure 9. This suggests that once the final mechanism is mobilized, fault deviation prevents any further localization. According to Figure 9 obviously deviation of the rupture plane to the left or right side of the tunnel will depend crucially on the location of the tunnel relative to the imposed rupture plane.

3.3.2 Effect of burial depth on fault–tunnel interaction

To examine the effect of burial depth on fault–tunnel interaction, a centrifuge model test with test parameters similar

to test 3, minus the tunnel location changed to $X = 25$ mm and $Y = 75$ mm ($X = 2$ m and $Y = 6$ m at equivalent prototype scale), was conducted in test 5. The ratio of H_c/D was increased from 0.92 to 2.03. As shown in Figure 10 (test 5), the burial depth of the tunnel strongly impacts the surface fault rupture and rupture path. In test 5, the tunnel location is close to the fault tip, and the right rupture reaches the soil surface. In test 3, the right rupture was placed 112.5 mm farther from the fault tip, whilst in test 5, the right rupture distance was increased to 126.5 mm farther from the fault tip.

However, for the final fault throw of $h/H = 0.25$ ($h = 50$ mm at model scale), three rupture planes were formed. Unlike test 3, the right side rupture plane reached the ground surface with the angle of about 40°, while the left side rupture plane didn't reach to the ground surface.

Ground surface measurements in Figure 10 indicate that the W/H is approximately 0.633 for the deep tunnel ($H_c/D = 2.03$), while the W/H for the shallow tunnel ($H_c/D = 0.92$) on the ground surface is 0.587. Furthermore, three distinct scarps appear on the ground surface at the final fault throw ($h/H = 0.25$).

The block within two main rupture planes is rotating clockwise and may also be subjected to some amount of shearing. This mechanism is facilitated by tunnel presence and could be considered as a force on the lining due to normal fault rupture. In other words, in normal faulting, increasing the height of the soil above the tunnel (H_c/D) is one of the factors that affect the propagation of the ruptures in the smaller zones towards the hanging wall, which is due to the tunnel presence.

The measurements also show that in test 3 with the ratio of H_c/D equal to 0.92 at $X = 55$ mm, $Y = 130$ mm, tunnel shifting after the ground rupture is smaller than that obtained for the tunnel with the ratio of H_c/D equal to 2.03 located at $X = 25$ mm, $Y = 100$ mm in test 5. The tunnel in test 5 is distinctly shifted downward with an almost 38.75 mm vertical displacement.

The differences in the tunnels and soil responses between tests 3 and 5 have revealed that tunnel location significantly influences the interaction between the fault and the tunnel. Further investigation is needed to study tunnel response in greater depth.

3.3.3 Effect of soil relative density (D_r) on fault–tunnel interaction

The soil parameters in test 4 were almost similar to those in test 3, with the exception that the soil relative density was reduced from 70% to 50% to examine the effect of soil relative density on fault–tunnel interaction (Figure 11). This density could be considered for loose to medium sand. Since the soil test with a relative density of 70% after two times repetition with a similar location of the tunnel to the test 4 has been failed, therefore test 4 has been compared to the test 3.
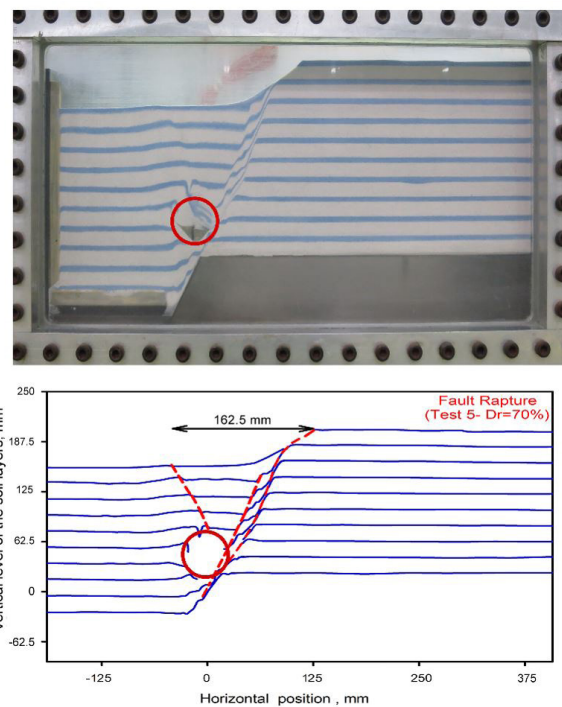
Figure 10. Effect of burial depth on fault tunnel interaction (test 5; $H_c/D = 2.03$; $X = 25$ mm; $Y = 75$ mm; $t = 1.2$ mm; $D = 49.4$ mm): Image of deformed soil specimen for the final fault throw; $h/H = 0.25$ ($D_r = 70\%$).
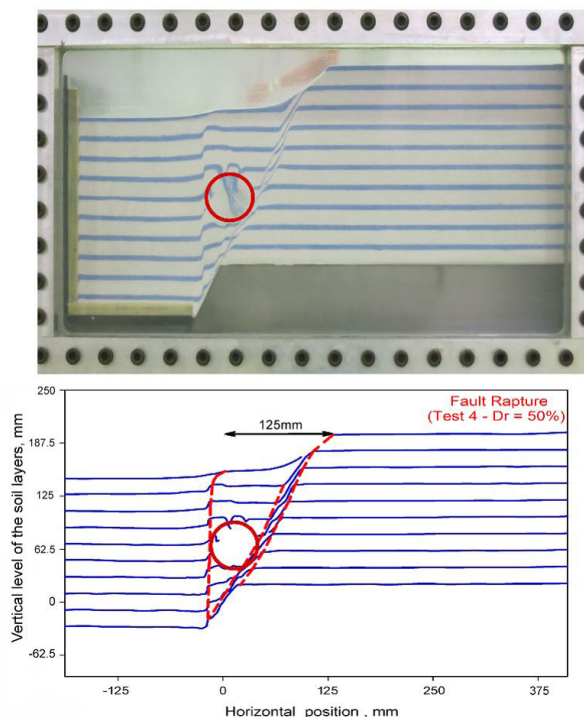
Figure 11. Effect of soil relative density on fault tunnel interaction (test 4; $H_c/D = 1.52$; $X = 40$ mm; $Y = 100$ mm; $t = 1.2$ mm; $D = 49.4$ mm): Image of deformed soil specimen for the final fault throw; $h/H = 0.25$ ($D_r = 50\%$).

As seen in Figure 11, the different relative density of the ground model with tunnel presence does not affect the number of rupture planes. The distance between the two rupture planes on the ground surface in test 4 with the ratio of $H_c/D = 1.52$ is about 125 mm. In addition, the tunnel in normal fault condition causes the fault movement to propagate to the ground surface and spread over a wider shear zone rather than a similar test with low relative density of dry sandy soil.

On the other hand, Figure 11 shows that the change in the model relative density as long as the tunnel straddled the line of the rupture plane gained from the free field tests (test 1 and test 2), has a different pattern of rupture plane developments. As seen, the model with 50% relative density generates three continuous rupture planes. While the left and right ruptures reach to the ground surface, the middle rupture does not reach to the soil surface. The underground tunnel causes the left rupture to bend and pass near the tunnel until it finally reaches the ground surface. Near the surface, the left rupture is inclined towards the footwall. Ground surface measurement also indicates that the ratio of W/H on the ground surface is approximately 0.75.

Although the final failure mechanisms of the lower relative density model were similar to those of the higher relative density model and a single strong discontinuity was deviated to the left edge of the tunnel, the high relative density model experienced a larger distance between the rupture planes. Once the final mechanism was formed ($h/H \approx 0.25$), the higher relative density model ($D_r = 70\%$) experienced a distance of 200 mm between the rupture planes, whereas the lower relative density model ($D_r = 50\%$) showed a distance of 125 mm. This distance between the rupture planes may cause considerable damage or even the collapse of the surface structures.

The vertical components of the surface deformations, measured by LDT analyses, are shown in Figure 12. This figure shows that the surface localization in the right side of the faulting zone for the $D_r = 50\%$ model is positioned 150 mm ($W/H = 0.75$) away from the fault tip and has a 47° angle on the soil surface, which is the same angle for the model with 70% soil relative density. Three distinct scarps were observed on the surface at the final fault throw of $h/H = 0.20$ ($h = 40$ mm at model scale) in test 3, while the number of scarps in test 4 at $h/H = 0.20$ were six. In addition, surface deformation of the lower relative density soil was more complex and less smooth than that of the higher relative density models. Due to the high number of localized deformations on the soil surface, is dangerous for surface structures.

3.3.4 Effect of tunnel rigidity (*EI*) on fault-tunnel interaction

To examine the effect of tunnel rigidity on fault–tunnel interaction, test 6 was conducted with similar conditions as test 5, except that the tunnel had slightly higher rigidity as
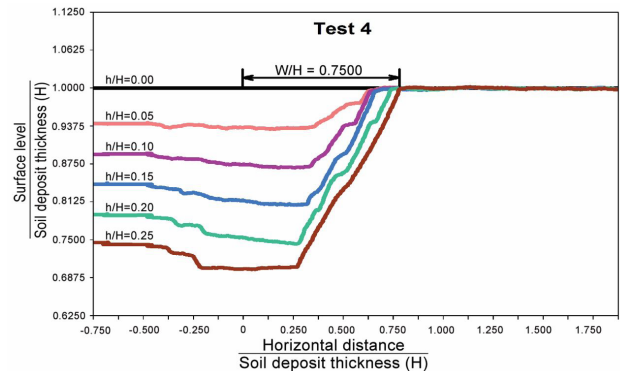
Figure 12. Effect of soil relative density on fault tunnel interaction: The ground surface level for different fault throws (test 4; $H_c/D = 1.52$; $X = 40$ mm; $Y = 100$ mm; $t = 1.2$ mm; $D = 49.4$ mm; $D_r = 50\%$).
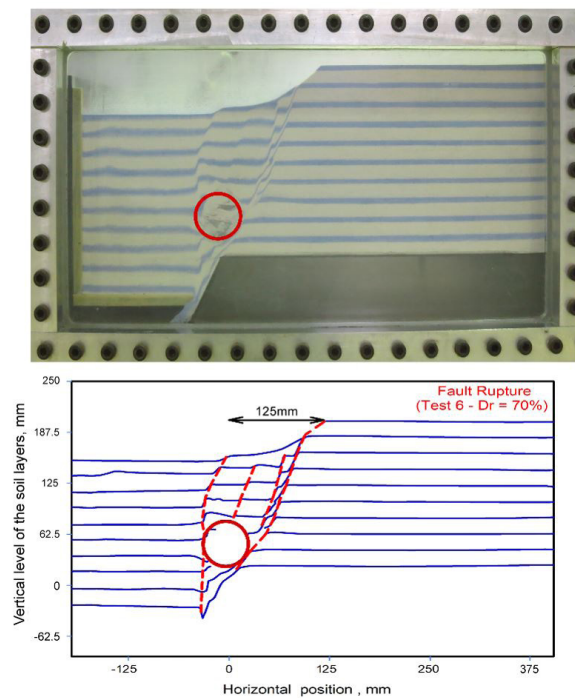
Figure 13. Effect of tunnel rigidity on fault tunnel interaction (test 6; $H_c/D = 2.01$; $X = 25$ mm; $Y = 75$ mm; $t = 1.4$ mm; $D = 49.8$ mm): Image of deformed soil specimen for the final fault throw; $h/H = 0.25$.

a result of increased diameter and thickness. The reason for choosing a slight increase in the diameter and thickness of the tunnel was to examine more accurately the process of changes in how the fault planes deviate.

Images, captured at the final stage of test 6 and shown in Figure 13, indicate clear localization at the soil surface for $h/H = 0.21$ ($h = 42.5$ mm at the model scale) on the right side of the tunnel. The rupture path on the left side of the tunnel towards the hanging wall also showed to have clear localization, but this rupture was more inclined to the footwall near the soil surface. Two shear localizations were observed for the ruptures on the right side, near the ground

surface. Therefore, it can be said that within the conditions of the tests performed, increasing the rigidity of a medium flexible tunnel changes the shear plane patterns and leaves the surface uneven. In fact, four shear planes were developed in the soil layer of the tunnel with higher rigidity. The distance between the two main rupture planes on the right side of the tunnel decreased as the tunnel rigidity was increased. The rigid tunnel increased the stresses placed on the soil beneath as a result of increasing both the shear strength and stiffness. It is obvious that parametric studies and repetition of different conditions will be needed to obtain general results. Test 6 showed that the left side of the rupture plane was also inclined towards the footwall, and the faulting zone was smaller than that of test 5. Figure 13 illustrate that an increase in the number of scarps on the soil surface, proving that fault localization, near the soil surface, increases in the presence of a tunnel with higher rigidity.

Figure 14 also presents that an initial localization was formed at the base towards the footwall in test 6. The second localization (also see Figure 13) propagated upwards from the right side of the tunnel until it formed a continuous shear plane. The third rupture plane was created from the top of the tunnel to the soil surface, and the forth shear plane was deviated near the fault tip, before reaching the ground surface.

Tunnel rotation and movement for test 5 was qualitatively similar to the same values of test 6 at the final fault throw of $h/H = 0.25$. However, the final rotation of the medium flexible tunnel was 42°, as compared with the 38° of the tunnel with more rigidity. The difference in values could be explained by the slight differences in tunnel diameter or tunnel thickness.

The results of the rigid and medium flexible tunnels suggest that the kinematic restraint of the rigid tunnel alone is governed by the fault outcropping location and additional rupture plane developments.

4. Discussion and implications for design

Previous researchers have reported experimental studies, which helped to identify the most relevant aspects pertaining the normal faulting problem (Lee & Hamada, 2005; Bransby et al., 2008a; Loli et al., 2012). The results of the centrifuge model tests reported in the present study have confirmed the following findings:

Tunnels can deviate earthquake fault ruptures away from the fault tip and create additional rupture planes. Such phenomena should be considered for the design of surface structures.

In the case where the tunnel was located close to the surface, two fault rupture paths developed on the right side of the tunnel. Coming in contact with the tunnel, the rupture paths were bent by the underground tunnel; the two paths collided and a new rupture path was created in upward direction towards the hanging wall. This phenomenon led to the existence of three fault ruptures in the soil layer. The faulting zone at the soil surface affected a large area of
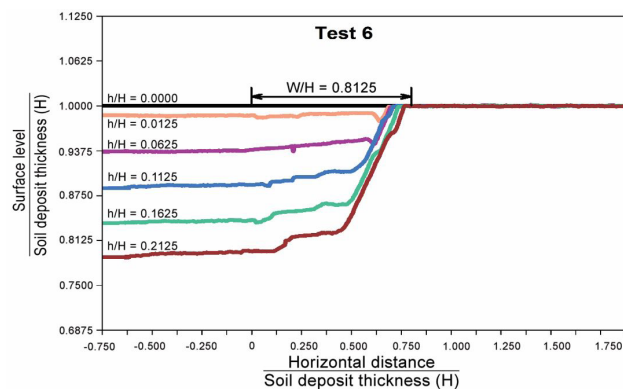
Figure 14. Effect of tunnel rigidity on fault tunnel interaction: The ground surface level for different fault throws (test 6; $H_c/D = 2.01$; $X = 25$ mm; $Y = 75$ mm; $t = 1.4$ mm; $D = 49.8$ mm).

the soil surface, which might be very dangerous for surface structures and should be considered in the design of such structures. The positions of the maximum surface gradient and surface displacement were changed as a result of the tunnel presence.

In the case where the tunnel was embedded in a deep soil layer, close to the fault tip and inside the faulting zone, the deep tunnel affected the displacement and deformation of the ground as well as the reduction of the faulting zone width within the overburden soil layer. Therefore, while increasing the tunnel depth minimized the faulting zone, the number of ruptures on the ground surface remained similar.

When the tunnel was embedded in loose sandy soil inside the faulting zone, the right and left side ruptures reached to the ground surface and the faulting zone width decreased. The number of scarps increased due to the presence of loose sandy soils. Further investigation is required to sufficiently understand the phenomena and develop general design methods.

Fault deviation in the case of the normal faulting was found to be more the result of tunnel rigidity than the kinematic restraint of the tunnel; a medium flexible tunnel behaved differently, compared with a higher rigidity tunnel. The rigid tunnel showed a different fault propagation pattern and the development of four shear planes. Movement and rotation of the tunnel cross section were similar to those of the medium flexible tunnels. The rigid tunnel increased the stresses placed on the soil beneath as a result of increasing both the shear strength and stiffness. The number of scarps on the ground surface also increased in the presence of the tunnel with higher rigidity. This suggests that the fault localization near the soil surface increases in the presence of a tunnel with high rigidity.

The results presented here indicate subtle interaction between the fault and the tunnel, which is sensitive to the burial depth of the tunnel, soil relative density and tunnel rigidity. All the tunnels, investigated in the present test series, caused the fault rupture path to deviate and create additional

rupture planes, but each tunnel underwent different amounts of rotation. Such rotations are enough to damage or destroy the tunnels.

Figure 15 plots three components of tunnel displacement against fault throw. The vertical and horizontal displacements of the tunnel suggest that the occurrence of the fault throw causes the tunnel to move downward. This was confirmed by the measurements of the tunnel displacements and rotations obtained in the first and final steps of the tests.
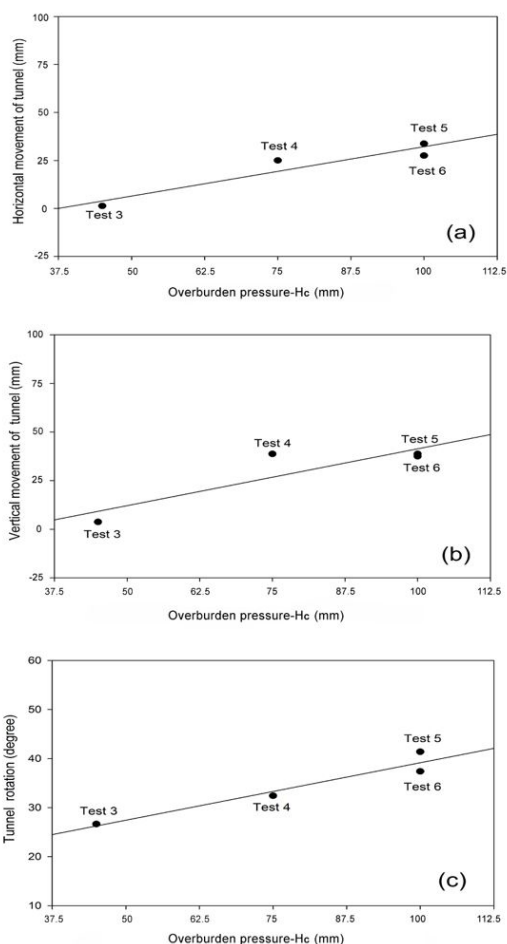
Figure 15. Tunnel movement against overburden pressure for the final fault throw; $h/H = 0.25$ (a) Horizontal movement of the tunnel (b) Vertical movement of the tunnel (c) Tunnel rotation.

Tunnel movement increases with increasing an overburden pressure (H_c) on the tunnel, which is embedded near the faulting zone. The tunnel rotation and movement for a low rigidity tunnel was qualitatively similar to the rigid one for the final fault throw ($h/H = 0.25$).

Table 4 compares the characteristics of the ruptures, both with and without the tunnel presence after the final fault throw by referring to the test 1 and test 2. As evident, while tunnel presence decreased the maximum surface gradient, it increased the number of scarps on the ground surface and the number of ruptures in the soil layer. Also it can be observed with the presence of tunnel when the tunnel overburden pressure (H_c) increased, the width of the distorted outcrop (W) and the number of scarps increased. As well at the same overburden depth, with increasing the tunnel rigidity, the width of distorted surface (W), the number of scarps and the number of ruptures increased.

5. Conclusions

This research aimed to analyze the interaction between normal faulting and tunnel in dry sandy soils for the first time using NCU geotechnical centrifuge equipment. After understanding this phenomenon, using present centrifuge tests, and then numerical and parametric studies some design recommendations can be documented. In this study the propagation of a normal fault in the free-field conditions was similar to that observed by previous researchers. A progressive localization of shear deformation running from the base of the soil layer up to the ground surface was observed. Once this localization reached to the soil surface, no further deformation of the soil occurred outside the faulting zone. The following results were obtained from the conditions of the centrifuge tests performed:

1. Tunnels caused the earthquake fault ruptures to deviate away from the paths observed in the free field tests and also created additional rupture planes (similar to the reverse fault tests conducted by the researchers of the present paper (Baziar et al., 2014, 2016, 2020)). Although this test and the aforementioned reverse fault tests confirm that fault deviation is possible due to the presence of a shallow tunnel, a single test

Table 4. Characteristics of ruptures with and without the presence of tunnel after the final fault throw ($h = 50$mm).

Test Condition	Test Number	H_c/D	W/H	Number of ruptures	Number of scarps	Maximum surface gradient (degree)	Affected width on the soil surface $/H$
Free field ($D_r = 50\%$)	1	-	0.75	2	2	33	1.156
Free field ($D_r = 70\%$)	2	-	0.687	2	2	37	1.218
Effect of shallow tunnel	3	0.92	0.587	3	3	35	1.250
Effect of deep tunnel	5	2.03	0.633	3	4	30	1.062
Effect of soil density	4	1.52	0.75	3	6	30	1.250
Effect of tunnel rigidity	6	2.01	0.812	4	5	29	1.062

is not enough to validate such claim. Consequently, further tests were carried out to investigate whether the deviation was caused by tunnel presence. Because of centrifuge tests are too expensive, more parametric studies are needed by numerical analysis, which could be verified with the test results of normal faulting;

2. Embedding the tunnel in a soil layer increased the number of scarps and differential displacements (slope) of the ground surface. This increase of differential displacement was highlighted with a larger increase in the fault displacement;

3. The position of the fault relative to the tunnel appeared to be considered in the interaction response. Hence, a range of possible fault positions should be considered in the design and in the parametric studies if the fault position is uncertain;

4. Surface deformation of the lower relative density soil was more complex and less smooth than that of the higher relative density models. Due to the high number of localized deformations on the soil surface, is dangerous for surface structures. The number of scarps increased due to the presence of loose sandy soils. Further parametric studies are required to sufficiently understand the phenomena and develop general design methods;

5. All the tested tunnels underwent significant rotation and displacement. This rotation appeared to increase with increasing the burial depth;

6. A rigid tunnel was also able to deviate the earthquake fault ruptures from the paths observed in the medium flexible tunnel test. The rotation and displacement of both rigid and flexible tunnels were almost similar;

7. For all of the tunnels investigated here, the additional fault rupture plane compared with the free field condition was developed on the left side of the tunnel.

Declaration of interest

The authors declare that they have no known competing financial interests or personal relationships that could have appeared to influence the work reported in this paper.

Authors' contributions

Ali Nabizadeh: supervision, writing - review & editing. Alireza Seghateh Mojtahedi: writing - original draft, writing - review & editing, data curation.

List of symbols

α Dip angle of the fault plane
H_c Burial depth of tunnel (overburden pressure)
D Diameter of the tunnel
t Thickness of the tunnel

D_r Relative density
E Young's modulus
G Shear modulus
G_s Specific gravity
ϕ Friction angle
H Height of soil deposit
h Vertical offset of the fault
γ Unit weight
W Distance from the fault tip to the location of the right side surface outcropping

References

Agalianos, A., Coquereaumont, O.D.C.D., & Anastasopoulos, I. (2020). Rigid slab foundation subjected to strike-slip faulting: mechanisms and insights. *Geotechnique*, 70(4), 354-373. http://dx.doi.org/10.1680/jgeot.18.P.280.

Ahmed, W., & Bransby, M.F. (2009). Interaction of shallow foundations with reverse faults. *Journal of Geotechnical and Geoenvironmental Engineering*, 135(7), 914-924. http://dx.doi.org/10.1061/(ASCE)GT.1943-5606.0000072.

Anastasopoulos, I. (2005). *Fault rupture-soil-foundation-structure interaction* [Ph.D. dissertation]. School of Civil Engineering, National Technical University.

Anastasopoulos, I., & Gazetas, G. (2007a). Foundation-structure systems over a rupturing normal fault: Part I. Observations after the Kocaeli 1999 earthquake. *Bulletin of Earthquake Engineering*, 5(3), 253-275. http://dx.doi.org/10.1007/s10518-007-9029-2.

Anastasopoulos, I., & Gazetas, G. (2007b). Foundation-structure systems over a rupturing normal fault: part II. Analysis of the Kocaeli case histories. *Bulletin of Earthquake Engineering*, 5(3), 277-301. http://dx.doi.org/10.1007/s10518-007-9030-9.

Anastasopoulos, I., Gazetas, G., Bransby, M.F., Davies, M.C.R., & Elnahas, A. (2007). Fault rupture propagation through sand: finite-element analysis and validation through centrifuge experiments. *Journal of Geotechnical and Geoenvironmental Engineering*, 133(8), 943-958. http://dx.doi.org/10.1061/(ASCE)1090-0241(2007)133:8(943).

Anastasopoulos, I., Kourkoulis, R., Gazetas, G., & Tsatsis, A. (2013). Interaction of piled foundation with a rupturing normal fault. *Geotechnique*, 63(12), 1042-1059. http://dx.doi.org/10.1680/geot.12.P.114.

Baziar, M.H., Nabizadeh, A., & Jabbary, M. (2012). Evaluation of Fault-foundation interaction using numerical studies. In *Proceedings of the 15th World Conference on Earthquake Engineering*, Lisbon, Portugal.

Baziar, M.H., Nabizadeh, A., & Jabbary, M. (2015). Numerical modeling of interaction between dip slip fault and shallow foundation. *Bulletin of Earthquake Engineering*, 13(6), 1613-1632. http://dx.doi.org/10.1007/s10518-014-9690-1.

Baziar, M.H., Nabizadeh, A., Khalafian, N., Lee, C.J., & Hung, W.Y. (2020). Evaluation of reverse faulting effects on the mechanical response of tunnel lining using

centrifuge tests and numerical analysis. *Geotechnique*, 70(6), 490-502. http://dx.doi.org/10.1680/jgeot.18.P.019.

Baziar, M.H., Nabizadeh, A., Jung Lee, C., & Yi Hung, W. (2014). Centrifuge modeling of interaction between reverse faulting and tunnel. *Soil Dynamics and Earthquake Engineering*, 65, 151-164. http://dx.doi.org/10.1016/j.soildyn.2014.04.008.

Baziar, M.H., Nabizadeh, A., Mehrabi, R., Lee, C.J., & Hung, W.Y. (2016). Evaluation of underground tunnel response to reverse fault rupture using numerical approach. *Soil Dynamics and Earthquake Engineering*, 83, 1-17. http://dx.doi.org/10.1016/j.soildyn.2015.11.005.

Bransby, M.F., Davies, M.C.R., Elnahas, A., & Nagaoka, S. (2008a). Centrifuge modeling of normal fault-foundation interaction. *Bulletin of Earthquake Engineering*, 6(4), 585-605. http://dx.doi.org/10.1007/s10518-008-9079-0.

Bransby, M.F., Davies, M.C.R., Elnahas, A., & Nagaoka, S. (2008b). Centrifuge modeling of reverse fault-foundation interaction. *Bulletin of Earthquake Engineering*, 6(4), 607-628. http://dx.doi.org/10.1007/s10518-008-9080-7.

Bray, J.D., & Kelson, K.I. (2006). Observations of surface fault rupture from the 1906 earthquake in the context of current practice. *Earthquake Spectra*, 22(52), 569-589. http://dx.doi.org/10.1193/1.2181487.

Cai, Q.P., Peng, J.M., Ng, C.W.W., Shi, J.W., & Chen, X.X. (2019). Centrifuge and numerical modelling of tunnel intersected by normal fault rupture in sand. *Computers and Geotechnics*, 111, 137-146. http://dx.doi.org/10.1016/j.compgeo.2019.03.010.

Faccioli, E., Anastasopoulos, I., Gazetas, G., Callerio, A., & Paolucci, R. (2008). Fault rupture–foundation interaction: selected case histories. *Bulletin of Earthquake Engineering*, 6(4), 557-583. http://dx.doi.org/10.1007/s10518-008-9089-y.

Ghadimi Chermahini, A., & Tahghighi, H. (2019). Numerical finite element analysis of underground tunnel crossing an active reverse fault: a case study on the Sabzkouh segmental tunnel. *Geomechanics and Geoengineering*, 14(3), 155-166. http://dx.doi.org/10.1080/17486025.2019.1573323.

Johansson, J., & Konagai, K. (2004). Fault induced permanent ground deformations-Simulations and experimental verification. In *Proceedings of the 13th World Conference on Earthquake Engineering* (Paper No. 479), Vanvouver, B.C., Canada.

Johansson, J., & Konagai, K. (2006). Fault induced permanent ground deformations an experimental comparison of wet and dry soil and implications for buried structures. *Soil Dynamics and Earthquake Engineering*, 26(1), 45-53. http://dx.doi.org/10.1016/j.soildyn.2005.08.003.

Johansson, J., & Konagai, K. (2007). Fault induced permanent ground deformations: experimental verification of wet and dry soil, numerical findings' relation to field observations of tunnel damage and implications for design. *Soil Dynamics and Earthquake Engineering*, 27(10), 938-956. http://dx.doi.org/10.1016/j.soildyn.2007.01.007.

Kelson, K.I., Kang, K.H., Page, W.D., Lee, C.T., & Cluff, L.S. (2004). Representative styles of deformation along the Chelungpu fault from the 1999 Chi-Chi (Taiwan) earthquake: geomorphic characteristics and responses of man-made structures. *Bulletin of the Seismological Society of America*, 91(5), 930-952. http://dx.doi.org/10.1785/0120000741.

Kiani, M., Akhlaghi, T., & Ghalandarzadeh, A. (2016). Experimental modeling of segmental shallow tunnels in alluvial affected by normal faults. *Tunnelling and Underground Space Technology*, 51, 108-119. http://dx.doi.org/10.1016/j.tust.2015.10.005.

Konagai, K., et al. (2007). *Annual report of the research and development program for resolving Critical Issues, Earthquake damage in active-faulting areas: creation of a comprehensive data archive and suggestions for its application to remedial measures for civil infrastructure systems*. Special Coordination Funds for Promoting Science and Technology, Ministry of Education, Culture, Sports, Science and Technology.

Lee, C.J., Wang, C.R., Wei, Y.C., & Hung, W.Y. (2012). Evolution of the shear wave velocity during shaking modeled in centrifuge shaking table tests. *Bulletin of Earthquake Engineering*, 10(2), 401-420. http://dx.doi.org/10.1007/s10518-011-9314-y.

Lee, C.J., Wu, B.R., Chen, H.T., & Chiang, K.H. (2006). Tunnel stability and arching effects during tunneling in soft clayey soil. *Tunnelling and Underground Space Technology*, 21(2), 119-132. http://dx.doi.org/10.1016/j.tust.2005.06.003.

Lee, W.J., & Hamada, M. (2005). An experimental study on earthquake fault rupture propagation through a sandy soil deposit. *Journal of Structure Engineering and Earthquake Engineering*, 22, 1-13. http://dx.doi.org/10.2208/jsceseee.22.1s.

Lin, M.L., Chung, C.F., Jeng, F.S., & Yao, T.C. (2007). The deformation of overburden soil induced by thrust faulting and its impact on underground tunnels. *Engineering Geology*, 92(3-4), 110-132. http://dx.doi.org/10.1016/j.enggeo.2007.03.008.

Loli, M., Bransby, M.F., Anastasopoulos, I., & Gazetas, G. (2012). Interaction of caisson foundations with a seismically rupturing normal fault: centrifuge testing versus numerical simulation. *Geotechnique*, 62(1), 29-43. http://dx.doi.org/10.1680/geot.9.P.153.

Loukidis, D., Bouckovalas, G., & Papadimitriou, A. (2009). Analysis of fault rupture propagation through uniform soil cover. *Soil Dynamics and Earthquake Engineering*, 29(11-12), 1389-1404. http://dx.doi.org/10.1016/j.soildyn.2009.04.003.

Mortazavi Zanjani, M., & Soroush, A. (2019). Numerical modelling of fault rupture propagation through layered sands. *European Journal of Environmental and Civil*

Engineering, 23(9), 1139-1155. http://dx.doi.org/10.1080/19648189.2017.1344148.

Naeij, M., Soroush, A., & Javanmardi, Y. (2019). Numerical investigation of the effects of embedment on the reverse fault-foundation interaction. *Computers and Geotechnics*, 113, 103098. http://dx.doi.org/10.1016/j.compgeo.2019.103098.

Oettle, N.K., & Bray, J.D. (2013). Fault rupture propagation through previously ruptured soil. *Journal of Geotechnical and Geoenvironmental Engineering*, 139(10), 1637-1647. http://dx.doi.org/10.1061/(ASCE)GT.1943-5606.0000919.

Prentice, C., & Ponti, D. (1997). Coseismic deformation of the Wrights tunnel during the 1906 San Francisco earthquake: A key to understanding 1906 fault slip and 1989 surface ruptures in the southern Santa Cruz Mountains, California. *Journal of Geophysical Research*, 102(B1), 635-648. http://dx.doi.org/10.1029/96JB02934.

Rasouli, H., & Fatahi, B. (2019). A novel cushioned piled raft foundation to protect buildings subjected to normal fault rupture. *Computers and Geotechnics*, 106, 228-248. http://dx.doi.org/10.1016/j.compgeo.2018.11.002.

Russo, M., Germani, G., & Amberg, W. (2002). Design and construction of large tunnel through active faults: a recent application. In *Proceedings of the International Conference of Tunnelling and Underground Space Use* (pp. 16-18), Istanbul, Turkey.

Tali, N., Lashkaripour, G.R., Hafezi Moghadas, N., & Ghalandarzadeh, A. (2019). Centrifuge modeling of reverse fault rupture propagation through single-layered and stratified soil. *Engineering Geology*, 249, 273-289. http://dx.doi.org/10.1016/j.enggeo.2018.12.021.

Thebian, L., Najjar, S., Sadek, S., & Mabsout, M. (2018). Numerical investigation of dip-slip fault propagation effects on offshore seabed sediments. *Engineering Geology*, 237, 149-167. http://dx.doi.org/10.1016/j.enggeo.2018.02.008.

Tsai, C.-C., Meymand, P., Dawson, E., & Wong, S.A. (2015). Behaviour of segmental pipeline protective vaults subjected to fault offset. *Structure and Infrastructure Engineering*, 11(10), 1369-1389. http://dx.doi.org/10.1080/15732479.2014.964733.

Tsatsis, A., Loli, M., & Gazetas, G. (2019). Pipeline in dense sand subjected to tectonic deformation from normal or reverse faulting. *Soil Dynamics and Earthquake Engineering*, 127, 105780. http://dx.doi.org/10.1016/j.soildyn.2019.105780.

Ulusay, R., Aydan, O., & Hamada, M. (2001). The behavior of structures built on active fault zones: examples from the recent earthquakes in Turkey. In *Workshop on Seismic Fault-Induced Failures: Possible Remedies for Damage to Urban Facilities* (pp. 1-26), Japan.

Wang, L. (2008). The characteristics of disasters induced by the Wenchuan Mw 8.0 Earthquake. In S. Prakash (Ed.), *International Conference on Case Histories in Geotechnical Engineering*, Washington, DC.

Wang, W.L., Wang, T.T., Su, J.J., Lin, C.H., Seng, C.R., & Huang, T.H. (2001). Assessment of damages in mountain tunnels due to the Taiwan Chi-Chi Earthquake. *Tunnelling and Underground Space Technology*, 16(3), 133-150. http://dx.doi.org/10.1016/S0886-7798(01)00047-5.

Yilmaz, M.T., & Paolucci, R. (2007). Earthquake fault rupture-shallow foundation interaction in undrained soils: a simplified analytical approach. *Earthquake Engineering & Structural Dynamics*, 36(1), 101-118. http://dx.doi.org/10.1002/eqe.625.